# DNS of gas bubbles behaviour using an improved 3D front tracking model—Model development

W. Dijkhuizen, I. Roghair, M. Van Sint Annaland *, J.A.M. Kuipers

*Institute of Mechanics, Processes and Control Twente (IMPACT), Faculty of Science and Technology, University of Twente, P.O. Box 217, 7500 AE Enschede, The Netherlands*

A B S T R A C T

In recent years CFD has proven to be a valuable and powerful tool to advance our understanding of complex multiphase flow systems arising in industrial applications. However, the predictive capabilities of this tool are determined by many factors of physical and numerical origin but in particular by the quality of the closures adopted for the description of the interface forces. The objective of this study is to improve the front tracking method in order to compute such forces with sufficient accuracy. This paper describes the further development of a 3D front tracking model to achieve improved volume conservation and circumvent problems related to the representation of surface tension. First, we have included a method to handle the pressure jump at the interface. This causes the spurious currents, observed in conventional front tracking, to decrease with two orders of magnitude. Also the advection scheme has been adapted, using higher order velocity interpolation (using cubic splines), and Runge–Kutta time-stepping, in order to prevent considerable volume changes of the dispersed phase. Test simulations involving a stationary bubble, a standard advection test and an oscillating droplet, demonstrate the effect of these improvements. The implementation of these procedures enlarged the computational window and in particular enabled the simulation of very small bubbles, where large surface forces dominate, without any significant spurious currents or volume loss.

© 2009 Elsevier Ltd. All rights reserved.

## 1. Introduction

### 1.1. Direct numerical simulations

The study of multiphase flows is extremely challenging due to the inherent complexities that arise when two or more different phases interact with each other. A key element of this field of research concerns the description of the interaction between phases that are separated by a deformable interface. In this respect, the description of a rising bubble through a liquid has received much attention. Traditionally, one would rely on analytical solutions or on empirical correlations obtained from time-consuming experiments, however due to the advent of CFD, powerful alternative approaches have become available such as direct numerical simulation (DNS).

For multiphase flows with deformable interfaces, many different DNS models have been reported in literature. These methods have their own strong and weak points. A brief overview will be given here, but for a more thorough overview the interested reader is referred to van Sint Annaland et al. (2006).

The main difference between the methods is in the description of the phase boundaries: while the level-set (LS), volume of fluid (VOF) and lattice Boltzmann (LB) models all capture the interface using data from the fixed grid, the front tracking (FT) model tracks the interface explicitly using a Lagrangian surface mesh. As a consequence, the LS, LB and VOF models exhibit automatic—potentially unphysical—coalescence when two bubbles are in close proximity. Additional measures in such codes can prevent this behaviour. In contrast, the FT model needs a sub-grid model to *allow* bubbles to merge (or breakup). For example, Singh and Shyy (2007) can change the topology of two separate interface meshes to a single mesh (coalescence) based on the phase fraction that is observed by two "probes" normal to each mesh cell. However, without such functionality, the front tracking method is uniquely qualified for studying swarm effects. Secondly, the superior interface resolution of the FT model is potentially more accurate in the description of surface tension forces. Of course FT also has some drawbacks, most notably the fact that the volume of the dispersed phases is not intrinsically conserved. Also, the need for restructuring the interface mesh is generally regarded as a drawback in literature. The main challenges for DNS are related to the treatment of the surface tension force, large density jumps at the interface and high Reynolds numbers, which can all be found in the important air/water system. A high surface tension force (small bubbles) produces unphysical velocity vectors

* Corresponding author. Tel.: +31 53 489 4478; fax: +31 53 489 2882.
  *E-mail address:* M.vanSintAnnaland@utwente.nl (M.V. Annaland).

(see Fig. 9, left), often referred to as parasitic or spurious currents, which may lead to excessive volume loss or other instabilities. For instance, using a front-tracking code based on the technique as given by Unverdi and Tryggvason (1992), an air bubble with a diameter of 1 mm in water cannot be simulated due to severe volume losses. While other DNS models do conserve the bubble volume, they are usually plagued by even stronger numerical stability problems, making it extremely difficult, if not impossible, to carry out these simulations. As a consequence Scardovelli and Zaleski (1999) and Zaleski (2005) concluded that there is no three-dimensional calculation of a falling drop or rising bubble for the difficult air/water conditions.

### 1.2. Objectives

In this article, an improved 3D front tracking model is described. Dedicated test-cases are used to assess the accuracy of the numerical results using analytical solutions and the performance is compared to other front tracking models reported in the literature. Moreover, benchmarks are used to find the optimal computational settings. From literature it is well-known that this type of model is often plagued by spurious currents and volume conservation issues. Therefore, several improvements have been made to enable the simulation of even very small bubbles or droplets with very high surface tension forces. First of all, a new method to account for the pressure jump at the bubble interface is implemented, which reduces the magnitude of the spurious currents by two orders of magnitude. Secondly, in order to further improve volume conservation and interface smoothness, the numerical implementation of the advection of the interface has been upgraded with higher order interpolation and time stepping methods. Finally, a novel and efficient way of computing the phase fractions is proposed, which circumvents the solution of a Poisson equation for the phase fractions.

In the following sections, first of all the 3D front tracking model will be described, with the improvements given in more detail. Then, the improvements are benchmarked using a variety of test-cases.

## 2. Improved 3D front tracking model

Compared to other DNS techniques, front tracking (FT; a.o. Unverdi and Tryggvason, 1992) offers a potentially more accurate surface tension treatment, because of the sub-grid interface resolution. In addition, the explicit interface tracking prevents unphysical coalescence of bubbles, which is particularly important when studying bubble swarms. However, FT also has some drawbacks, most notably the fact that the volume conservation of the dispersed elements is not intrinsically enforced. Also, the need for restructuring the interface grid ("remeshing") is generally regarded as a drawback in literature.

In this article a standard 3D FT model (van Sint Annaland et al., 2006) has been improved, to allow the simulation of even very small bubbles, with very high surface tension forces, without numerical problems such as volume loss and spurious currents. More specifically, the following modifications have been implemented:

- Direct coupling between the surface tension force and the pressure jump at the interface, to reduce the magnitude of spurious currents while maintaining a sharp interface representation.
- Direct calculation of the phase fractions from the interface triangulation, eliminating the standard, but computationally expensive solution of the Poisson equation for the phase fractions proposed by Unverdi and Tryggvason (1992).

- Higher order advection of the interface, to reduce volume conservation errors and improve interface smoothness.
- Semi-implicit treatment of the stress tensor, avoiding time step limitations for highly viscous flows.

In the following paragraphs a general description of the FT model is given, with the improvements worked out in more detail. Subsequently, the improved model will be validated and bench-marked using a collection of dedicated test cases.

### 2.1. Governing equations and numerical solution method

The Front Tracking model is based on the incompressible Navier–Stokes equations, with a singular source-term $\mathbf{F}_\sigma$ for the surface tension force at the interface:

$$\rho \frac{\partial \mathbf{u}}{\partial t} = -\nabla p - \rho \nabla \cdot (\mathbf{u}\mathbf{u}) - \nabla \cdot \boldsymbol{\tau} + \rho \mathbf{g} + \mathbf{F}_\sigma \tag{1}$$

where $\mathbf{u}$ is the velocity field, $\boldsymbol{\tau}$ the stress tensor and $p$ the pressure field. Mass conservation is enforced by the continuity equation:

$$\nabla \cdot \mathbf{u} = 0 \tag{2}$$

Since the velocity field is continuous even across interfaces for gases and liquids, a one-field formulation can be used to describe all phases at once. However, the shear stress and pressure are not continuous across the interface and the usual jump condition is given by Eq. (3). The physical properties (viz. density $\rho$ and dynamic viscosity $\eta$) also change discontinuously across the interface. How these physical properties are calculated will be explained in Section 2.6.

$$[-p\mathbf{I} - \boldsymbol{\tau}] \cdot \mathbf{n} = \mathbf{F}_\sigma \cdot \mathbf{n} \tag{3}$$

The interface is represented (parameterised) by an unstructured grid of triangular markers, with the Lagrangian (control) points situated on the corners of the markers. The Lagrangian points are co-moving with the fluid, the triangular markers are merely a result of the logical connection between the control points.

For each time step the following procedure is carried out: first, the Navier–Stokes equations together with the continuity equation are solved with a fractional step projection method to obtain the flow field. Then, the front (interface) is moved to its new location, using locally interpolated velocities, after which the surface grid is restructured (if necessary) and the physical properties are updated (see Dijkhuizen, 2008). The system of equations is solved on a Cartesian staggered grid, using a fractional step method. First of all, an explicit estimate of the velocity $\mathbf{u}^{n^*}$ is calculated, using information from the previous time step (indicated with the superscript $n$):

$$\mathbf{u}^{n^*} = \mathbf{u}^n + \frac{\Delta t}{\rho} [-\nabla p - \nabla \cdot \mathbf{u}\mathbf{u} - \nabla \cdot \boldsymbol{\tau} + \rho \mathbf{g} + \mathbf{F}_\sigma]^n \tag{4}$$

The convective term is discretised with a second order flux-delimited Barton scheme (Centrella and Wilson, 1984) and the diffusion term with a second order central scheme. For highly viscous systems at small length scales, the time step $\Delta t$ can be limited by the stability of the explicit treatment of the diffusion terms, which is circumvented by treating part of the diffusion terms implicitly (following Uhlmann, 2005). Therefore, the stress tensor is split into an implicit part ($\boldsymbol{\tau}^{n^{**}}$), with all the derivatives containing the velocity component in one direction, and an explicit part ($\boldsymbol{\tau}^n$) containing the other velocity components (e.g. $u_y$ and $u_z$ when solving for $u_x$). We have confirmed that this gives us

the same solution in case a fully explicit treatment is used.

$$\boldsymbol{\tau} = \boldsymbol{\tau}^n + \boldsymbol{\tau}^{n**} = \begin{bmatrix} -2\eta\frac{\partial u_x^{n**}}{\partial x} & -\eta\left(\frac{\partial u_y^{n**}}{\partial x} + \frac{\partial u_x^n}{\partial y}\right) & -\eta\left(\frac{\partial u_z^{n**}}{\partial x} + \frac{\partial u_x^n}{\partial z}\right) \\ -\eta\left(\frac{\partial u_x^{n**}}{\partial y} + \frac{\partial u_y^n}{\partial x}\right) & -2\eta\frac{\partial u_y^{n**}}{\partial y} & -\eta\left(\frac{\partial u_z^{n**}}{\partial y} + \frac{\partial u_y^n}{\partial z}\right) \\ -\eta\left(\frac{\partial u_x^{n**}}{\partial z} + \frac{\partial u_z^n}{\partial x}\right) & -\eta\left(\frac{\partial u_y^{n**}}{\partial z} + \frac{\partial u_z^n}{\partial y}\right) & -2\eta\frac{\partial u_z^{n**}}{\partial z} \end{bmatrix}$$

(5)

Note that as a result of this partial implicit treatment, the stress tensor has lost its diagonal symmetry (i.e. $\tau_{zx} \neq \tau_{xz}$). These implicit terms have been chosen such that each velocity component can be solved separately and the remaining explicit terms are relatively small. For each velocity component this discretisation results in a seven-point stencil (Eq. (6)) and the three independent systems of linear equations (one for each velocity component) are solved sequentially using an efficient ICCG matrix solver.

$$u_x^{n**} = u_x^{n*} - \frac{\Delta t}{\rho}\left[-\frac{\partial}{\partial x}\left(2\eta\frac{\partial u_x^{n**}}{\partial x}\right) - \frac{\partial}{\partial y}\left(\eta\frac{\partial u_x^{n**}}{\partial y}\right) - \frac{\partial}{\partial z}\left(\eta\frac{\partial u_x^{n**}}{\partial z}\right)\right]$$

(6)

$$u_{x,i+\frac{1}{2}j,k}^{n**} = u_{x,i+\frac{1}{2}j,k}^{n*} + \frac{\Delta t}{\rho_{i+\frac{1}{2}j,k}}\left[2\eta_{i+1,j,k}\frac{u_{x,i+\frac{3}{2}j,k}^{n**} - u_{x,i+\frac{1}{2}j,k}^{n**}}{\Delta x^2}\right.$$

$$-2\eta_{i,j,k}\frac{u_{x,i+\frac{1}{2}j,k}^{n**} - u_{x,i-\frac{1}{2}j,k}^{n**}}{\Delta x^2} + \eta_{i+\frac{1}{2}j+\frac{1}{2},k}\frac{u_{x,i+\frac{1}{2}j+1,k}^{n**} - u_{x,i+\frac{1}{2}j,k}^{n**}}{\Delta x \Delta y}$$

$$-\eta_{i+\frac{1}{2}j-\frac{1}{2},k}\frac{u_{x,i+\frac{1}{2}j,k}^{n**} - u_{x,i+\frac{1}{2}j-1,k}^{n**}}{\Delta x \Delta y} + \eta_{i+\frac{1}{2}j,k+\frac{1}{2}}$$

$$\times\frac{u_{x,i+\frac{1}{2}j,k+1}^{n**} - u_{x,i+\frac{1}{2}j,k}^{n**}}{\Delta x \Delta z} - \eta_{i+\frac{1}{2}j,k-\frac{1}{2}}\frac{u_{x,i+\frac{1}{2}j,k}^{n**} - u_{x,i+\frac{1}{2}j,k-1}^{n**}}{\Delta x \Delta z}\right]$$

All the forces in the Navier–Stokes equations have now been accounted for; however the continuity equation has not yet been satisfied. This is done using a standard pressure correction step (Eq. (7)), which involves solving a linear system of equations with a hepta-diagonal matrix.
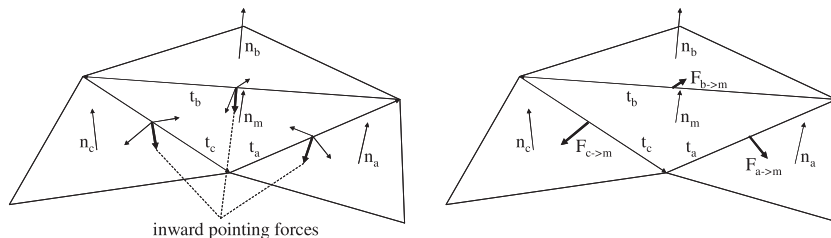
$$\delta p \equiv p^{n+1} - p^n \mathbf{u}^{n+1} = \mathbf{u}^{n**} - \frac{\Delta t}{\rho}\nabla(\delta p)$$

(7)

### 2.2. Surface tension force

One of the most widespread surface tension models for FT is based on the idea of pull-forces, which are computed directly from the triangular markers representing the interface. The individual pull-force of marker $a$ acting on marker $m$ can be computed from their normal vectors and joint tangent:

$$\mathbf{F}_{\sigma,a\to m} = \sigma(\mathbf{t}_{ma} \times \mathbf{n}_a)$$

(8)

There is however a subtle difference in the way the total force on a marker is calculated by different research groups (see Fig. 1). Shin and Juric (2002) first compute the net inwards pointing force on each tangent, which is defined as the sum of two pull forces.

These inward pointing forces are then distributed equally to both adjacent markers, leading to the following force on marker $m$:

$$\mathbf{F}_{\sigma,m} = \sum_i \mathbf{F}_{\text{inward},i} = \sum_{i=a,b,c}\frac{\mathbf{F}_{\sigma,m\to i} + \mathbf{F}_{\sigma,i\to m}}{2}$$

(9)

Alternatively, the sum of the pull-forces acting on the marker can be taken (Deen et al., 2004), which can be shown to give exactly the same solution since the forces tangential to the interface cancel each other out, yielding only an inward directed net force (Eq. (10)). Since this variation is much simpler and requires only half the computational work, it is used in this work. According to Tryggvason et al. (2001) this direct approach avoids the complicated and not very accurate polynomial interpolation of the surface in 3D. As a consequence complicated error-suppressing algorithms such as described by Singh and Shyy (2007) are also avoided. Finally, the total net surface tension force is automatically zero for a closed surface.

$$\mathbf{F}_{\sigma,m} = \frac{1}{2}\left(\sum_{i=a,b,c}\mathbf{F}_{\sigma,m\to i} + \sum_{i=a,b,c}\mathbf{F}_{\sigma,i\to m}\right) = \frac{1}{2}\sum_{i=a,b,c}\mathbf{F}_{\sigma,i\to m}$$

(10)

When the force on a marker has been calculated, a mass-weighing distribution function (Deen et al., 2004) is used to map the total force to the surrounding cells based on their density:

$$(\mathbf{F}_\sigma)_{i,j,k} = \frac{\sum_m \rho_{i,j,k} D(\mathbf{x}_{i,j,k} - \mathbf{x}_m)\mathbf{F}_{\sigma,m}}{\sum_m \rho_{i,j,k} D(\mathbf{x}_{i,j,k} - \mathbf{x}_m)}$$

(11)

$$D(\mathbf{r}) = d_x(r_x)\,d_y(r_y)\,d_z(r_z)$$

(12)

$$d_x(r_x) = \begin{cases} 1 - \dfrac{|r_x|}{h} & \text{if } |r_x| \leq h \\ 0 & \text{if } |r_x| > h \end{cases}$$

(13)

The physical background of this mass-weighing function is based on the continuity of velocity at the interface: a force which acts equally on the gas and on the liquid phase must yield the same velocity at the interface. Therefore the momentum should be balanced based on the density in the different cells, which reduces the magnitude of the spurious currents considerably and thus makes it possible to simulate systems with very high density ratios of up to $10^4$ without any numerical problems.

Other FT models described in literature typically alleviate this problem by smearing out the surface tension forces over a large stencil using e.g. a Peskin-like function (Tryggvason et al., 2001; Shin and Juric, 2002; Peskin, 1977). Also they have a density gradient over several cells at the interface, as a result of the way the phase fractions are calculated. This may allow them to simulate systems with moderately high surface tension forces or high density ratios, but at the cost of a sharp interface representation.



**Fig. 1.** Surface tension forces acting on a triangular marker. Shin and Juric (2002) use the net inwards pointing forces on each of the tangents (left), while Deen et al. (2004) use the pull-forces on the marker (right). It can be shown that both methods yield identical results, since the pull-forces in the plane of marker $m$ cancel each other out.

## 2.3. Interfacial pressure jump

The coupling between surface tension forces and the pressure jump at the interface is crucially important to prevent unphysical spurious currents, as was demonstrated by Popinet and Zaleski (1999) using a 2D front tracking model. They used a large computational stencil ($3 \times 3$ nodes) to accurately capture the pressure jump at the interface. However, this is not feasible in 3D, due to the resulting computationally prohibitive 27-band pressure matrix. Moreover, it is important to understand that interfacial tension creates a pressure discontinuity at the position of the front, which is not easily accounted for in the Eulerian framework, even with higher order discretisations. Our approach of handling the pressure jump is similar to that of Francois et al. (2006) and Renardy and Renardy (2002). The magnitude of the pressure jump related to the surface tension force can be calculated from the jump condition (Eq. (3)), when the shear stress in the normal direction is neglected this results in Eq. (14).

$$\int_{\partial S} [p]\, dS = \int_{\partial S} \mathbf{F}_\sigma \cdot \mathbf{n}[p] = \frac{\int_{\partial S} \mathbf{F}_\sigma \cdot \mathbf{n}}{\int_{\partial S} dS} = \frac{\sum_m \mathbf{F}_{\sigma,m} \cdot \mathbf{n}_m}{\sum_m S_m} \tag{14}$$

During the surface tension force calculation, which was described in the previous section, the surface tension force components obtained for each marker are summed to yield the total surface tension force over the entire bubble. By calculating the sum of the area of all markers, the interfacial area of the bubble is also known, and hence the pressure jump can be calculated (Eq. (14)). By distributing the total pressure jump over all markers, weighted by the marker area, we incorporate the pressure jump. Thus, we obtain a pressure jump term per interface marker, and we add this term to the right-hand side of the momentum equations (i.e. the equations for $u_x^{n^*}$, $u_y^{n^*}$ and $u_z^{n^*}$) in the same way the surface tension force was added (i.e. by mass-weighing; Eqs. (11)–(13)). Of course, the resulting force from the pressure jump works in the opposite direction with respect to the surface tension force. When we do this for all markers of a bubble, the pressure jump is equally distributed over the entire interface of the bubble, whereas the surface tension force is locally much higher in strongly curved parts of a bubble than a flattened part the interface. The advantage of using this technique with front-tracking is that the location of the interface is exactly known, and the surface tension force and pressure jump terms are mapped to this exact location (as opposed to front-capturing techniques as used by Francois et al., 2006 or Renardy and Renardy, 2002). The pressure jump and surface tension force cancel each other out for interfaces with a constant curvature (i.e. a sphere), and if the curvature varies over the interface, only a relatively small net force will be transmitted to the Euler grid. This is much more accurate than a purely Eulerian treatment of the pressure discontinuity, thereby leading to much lower spurious currents and improved numerical stability. All of this is realised with no additional computational cost, because the surface tension force has already been calculated.

## 2.4. Surface advection

de Sousa et al. (2004) mention that when the Reynolds number is high (Re > 50) small undulations may appear at the interface, which are "due to variations in the velocity field from cell to cell." The solution they present in their article is a filter to suppress these undulations. Instead of using a filter, in this work the focus is on tackling the cause of the disturbances, which is found to be primarily dominated by the advection of the surface grid.

Most front tracking models in literature utilise a first order velocity interpolation. The problem with this type of interpolation

is that it is piecewise linear, not providing a smooth transition between nodes. As a result the first order interpolation produces an imprint of the Euler grid on the bubble (Fig. 2, left). To keep the surface smooth, a higher order velocity interpolation is needed, for which a natural cubic spline (Press and Vetterling, 1992) is a good candidate since it guarantees a smooth interpolation and thus the bubble surface will stay smooth (Fig. 2, right). The spline is independent for each velocity component in every direction, because at the nodal points the interpolation matches the interpolated values exactly. This results in three independent tri-diagonal systems of equations, which can be solved very efficiently in $O(N)$ operations using a tri-diagonal algorithm. Of course the spline is not determined in the whole domain, but only in a small region around the dispersed elements. It was found that when using a box around the bubble, which is extended by 10 cells in each direction, the results were indistinguishable from a global spline (Fig. 3). The presence of other bubbles within the stencil still allows the splines to be determined, because both gas and liquid phase are calculated on the same flow field. Finally, to complement the higher order velocity interpolation, fourth order Runge–Kutta time-integration is used, which is capable of tracking highly curved velocity fields.
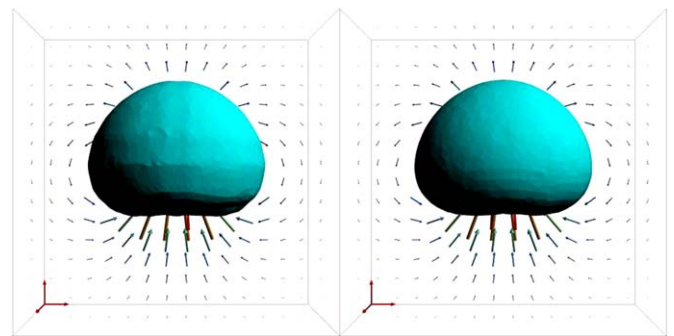
**Fig. 2.** Qualitative effect of the velocity interpolation on the surface grid for a 2 mm air bubble in water. It can be seen that the first order velocity interpolation creates imprints on the surface grid (left), while the higher order interpolation gives a smooth result (right). All other settings are identical.
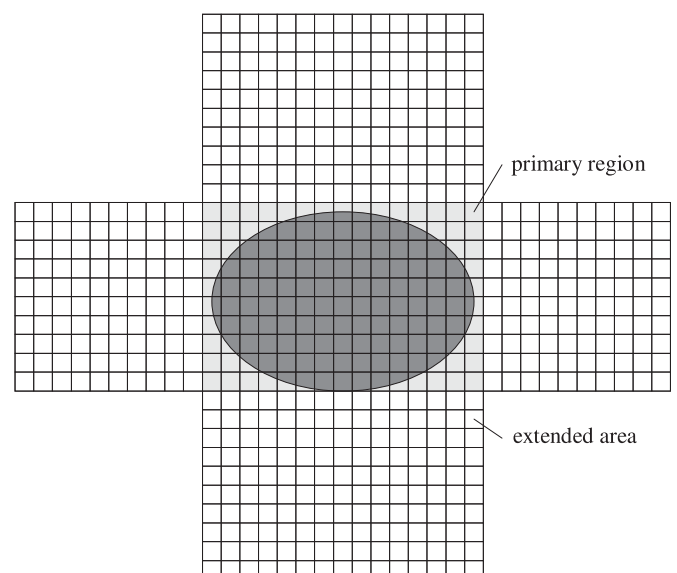
**Fig. 3.** Local region around the dispersed phase for calculating the cubic spline.

## 2.5. Remeshing

The restructuring of the front consists of two elementary operations: marker addition and removal. For both operations the length of the line segments is used as the criterion: when a line segment is too small, two markers are removed (Fig. 4). For a line segment which is longer than a prescribed value, an additional point is placed in the middle of the line segment and two extra markers are created. Generally, we use a maximum line segment of 0.4 times the Eulerian grid size, and a minimum of 0.2 times the Eulerian grid size.

Refining a marker involves the addition of a new Lagrangian control point on the line segment, and the connections between the control points are updated. This approach does not introduce any loss of volume, because the resulting new markers are exactly on top of the old marker. However, removing a control point because a line segment is too small causes the new, larger, marker to cut off the fine details of the interface that were represented by the small markers, hereby introducing volume defects (see Section 3.2).

## 2.6. Phase fraction calculation

Once the front has been moved, the phase fractions can be updated, in order to find the density and viscosity field. Traditionally the phase fractions $F_p$ are found by solving the following Poisson equation (Unverdi and Tryggvason, 1992), containing the interfacial gradient $\mathbf{G}_p$ that is calculated from the interface triangulation:

$$\nabla^2 F_p = \nabla \cdot \mathbf{G}_p \tag{15}$$

$$\mathbf{G}_p = \sum_{m \varepsilon p} D(\mathbf{x} - \mathbf{x}_m)\mathbf{n}_m S_m \tag{16}$$

The drawback of this method is that the gradient has to be distributed to the Eulerian grid and as a consequence, the phase fractions are smeared out. Secondly, the numerical scheme creates under- and overshoots, which affect the volume of the dispersed phase and have to be filtered out. Finally, solving an additional Poisson equation is computationally demanding, especially for large grids.

Therefore in this work a different method is introduced, which calculates the phase fractions directly from the location of the surface markers. It uses the triangular surface markers to calculate the volume in each cell piece by piece (Fig. 5). The calculation of the volume under a marker follows straight-
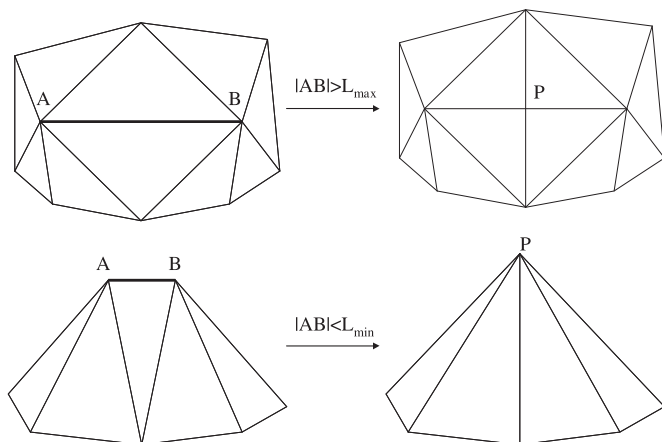


**Fig. 4.** Surface grid remeshing procedures for line segments which are either larger (top) or smaller than a set value (bottom).
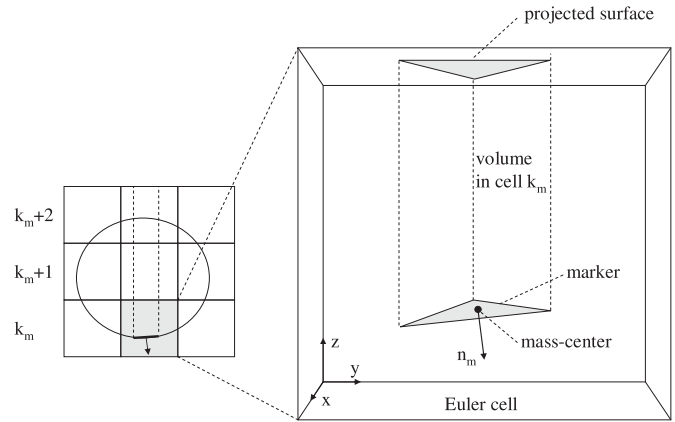


**Fig. 5.** Volume-integration in the novel phase fraction calculation. The volume above marker $m$ is added to or subtracted from cell $k_m$, depending on the direction of its normal vector. Other cells above that, all receive a contribution which corresponds to the surface area times the grid spacing.

forwardly from the location of its centre of mass in the $z$-direction $z_{m,c}$, the surface normal $\mathbf{n}_m$ and the surface area $S_m$:

$$V_m(i,j,k) = \begin{cases} (-\mathbf{e}_z \cdot \mathbf{n}_m)S_m(k\Delta z - z_{m,c}) & \text{if } k = k_m \\ (-\mathbf{e}_z \cdot \mathbf{n}_m)S_m\Delta z & \text{if } k > k_m \end{cases} \tag{17}$$

where the integration direction is arbitrarily chosen to be the $+z$ direction. Depending on the direction of the outwards pointing normal vector $\mathbf{n}_m$ the volume under the marker in a cell is either subtracted or added to the respective cell. After all the contributions from the markers of a bubble are added, only the volume inside the bubble remains (Fig. 6). Once the contribution of each marker is known, the phase fractions can be calculated by adding the contributions of all the markers in a cell belonging to phase $p$:

$$F_p(i,j,k) = \frac{1}{\Delta x \Delta y \Delta z} \sum_{m \varepsilon p} V_m(i,j,k) \tag{18}$$

The only remaining problem occurs when a marker occupies more than one cell. In this case the marker will have to be distributed over these respective cells, for which a "cutting" procedure is proposed (Fig. 7). The basis of this method is to cut each line segment if it crosses a cell boundary, consequently creating three smaller triangles.

Now that the phase fractions are known, the local density and viscosity can be calculated. For the density a standard volume-weighing method is used (Eq. (19)), while for the viscosity harmonic averaging is employed (Eq. (20)). According to Prosperetti (2002) the harmonic averaging significantly improves the continuity of tangential stress across the interface. Note that not only the calculation, but also the interpolation of the viscosity is carried out harmonically.

$$\rho(i,j,k) = \sum_{p=0}^{N_{ph}-1} F_p(i,j,k)\rho_p \tag{19}$$

$$\frac{\rho(i,j,k)}{\eta(i,j,k)} = \sum_{p=0}^{N_{ph}-1} F_p(i,j,k)\frac{\rho_p}{\eta_p} \tag{20}$$

## 3. Model validation

This section demonstrates the effect of the proposed modifications to the performance of the 3D FT model. First, the surface tension treatment is tested by comparing simulations to
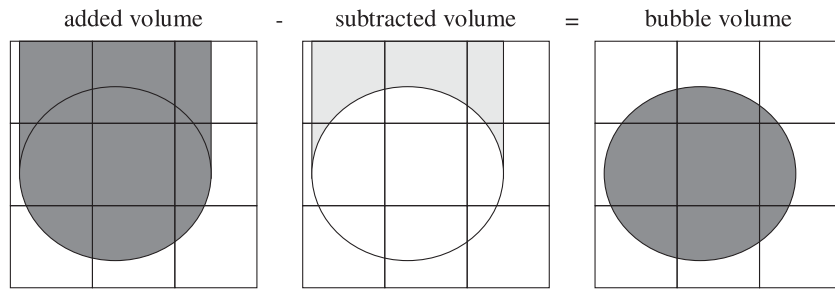
Fig. 6. Situation after all the contributions of the markers for a bubble have been collected. It can be seen that for the area above the bubble, the added volume cancels the subtracted volume out, so that the correct bubble volume is obtained.
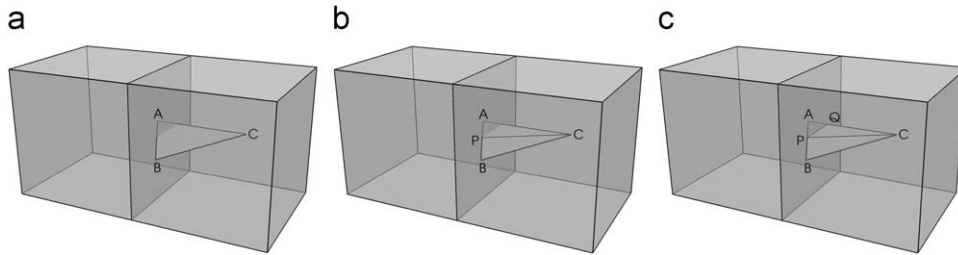


Fig. 7. Marker cutting procedure: (a) a marker with control points A, B and C is found in two adjacent Eulerian cells. Lines AB and AC need to be cut, (b) a point P is determined on the marker and the Eulerian cell faces. A line PC is constructed on line AB and (c) another point Q is determined on line AC. Since BC did not need to be cut, the operation is finished.

analytical results for a spherical, stationary bubble in a zero-gravity field. This case is followed by a standard advection test, which quantifies the error introduced by moving the front. Thirdly, the discretisation of the Navier–Stokes equations is verified by simulating an oscillating bubble with viscous damping and comparing with an analytical solution.

### 3.1. Stationary bubble

The improvement achieved by the new treatment of the pressure jump at the bubble surface is demonstrated for a spherical bubble of 1 mm in a zero-gravity environment (see Table 1). It is well-known that in this case there is an excess pressure inside the bubble, exactly counterbalancing the surface tension forces. As a result, a force balance gives the analytical value of the pressure jump:

$$\Delta p_{th} = \frac{4\sigma}{d} \qquad (21)$$

It can be seen that both the surface tension force and interfacial pressure jump are proportional to the surface tension coefficient and the inverse bubble diameter (curvature). This knowledge is used to define suitable dimensionless errors, which are completely independent of all physical properties and the bubble diameter. First of all, the $L_2$–error norm of the surface tension force on the individual markers is defined (Eq. (22)). Secondly, the error in the pressure jump can be directly compared to its theoretical counterpart (Eq. (23)). Fig. 8a clearly shows that the surface tension $L_2$–error norm decreases with order $\frac{1}{2}$, which can be explained by the fact that the accuracy of the pull-forces varies with the tangent length ($\sim 1/\sqrt{N_m}$), with $N_m$ the number of markers. On the other hand, the relative error in the pressure jump is several orders of magnitude lower and depends linearly on the number of markers, because it is a surface force.

$$E_\sigma = \sqrt{\frac{1}{N_m} \sum_{m=1}^{N_m} \frac{|\mathbf{F}_{\sigma,m} - \Delta p_{th} S_m \mathbf{n}_m|^2}{(\Delta p_{th} S_m)^2}} \qquad (22)$$

**Table 1**
Physical properties of the stationary bubble validation case.

| | | |
|---|---|---|
| Density gas phase $\rho_d$ | 1.25 | kg m$^{-3}$ |
| Density liquid phase $\rho_c$ | 1000 | kg m$^{-3}$ |
| Viscosity gas phase $\eta_d$ | $1.8 \times 10^{-5}$ | Pa s |
| Viscosity gas phase $\eta_c$ | $1 \times 10^{-3}$ | Pa s |
| Surface tension coefficient $\sigma$ | 0.073 | N m$^{-1}$ |
| Bubble diameter $d$ | $10^{-3}$ | m |
| Time step $\Delta t$ | $10^{-6}$ | s |
| Grid size $\Delta x, \Delta y, \Delta z$ | $5 \times 10^{-5}$ | m |
| Domain size | $40 \times 40 \times 40$ | Grid cells |

$$E_p = \frac{\Delta p_{sim} - \Delta p_{th}}{\Delta p_{th}} \qquad (23)$$

with $S_m$ the surface of marker $m$. The pressure jump in the simulations, $\Delta p_{sim}$, is obtained in the surface tension force calculations (see Section 2.3). When the surface tension force is calculated on a per-marker basis, a corresponding pressure jump can be obtained using Eq. (14). Summing the partial pressure jumps over all markers gives us the total pressure jump.

The mismatch between the surface tension force and interfacial pressure jump results in false momentum, which can also be quantified in a dimensionless form:

$$E_{momentum} = \frac{\Delta x}{\Delta t} \frac{\rho |\mathbf{u}|_{max}}{\Delta p_{th}} \qquad (24)$$

In Eq. (24), the term on the right results from the discretisation of the pressure-correction step, and $\rho$ represents the macroscopic density as given in Eq. (19). Fig. 8b shows that with the conventional treatment of the pressure jump the error is constant at approximately 4%. This proves that in traditional FT models, the treatment of the pressure jump using the Eulerian grid is the limiting factor and not the computation of the surface tension forces. Only with the new implementation to account directly for the pressure jump, does the error decrease first order with the number of markers. Note that the difference in errors between

cases where the bubble diameter is equal to 10 and 20 Eulerian cells is related to the smaller width of the distribution function at higher resolution. The error can be reduced again by using a larger stencil for mapping, however at the expense of the sharp-interface philosophy. It can be concluded that the typical improvement is about two orders of magnitude compared to a classical CSF method (Brackbill et al., 1992), which has been realised without the additional computational costs of a higher order pressure force discretisation (Scardovelli and Zaleski, 1999).

Note that the method of handling the pressure jump still does not eliminate the spurious currents *entirely* for a spherical bubble without external forcing; the triangular grid that represents the interface still is an *approximation* of the spherical shape and therefore suffers from a slight non-constant curvature. For the case of a 1 mm air bubble in water in zero-gravity, we thus find that the spurious current velocity $\mathbf{u}_{spurious}$ depends on the number of markers on the interface by $\mathbf{u}_{spurious} = O(N_m^{-1} - 1)\,[\mathrm{m\,s^{-1}}]$. This can also be seen from Fig. 8.

Finally, the steady-state magnitude of the spurious currents with viscous damping can be compared to literature values for full 3D simulations. The two sources found in literature (Table 2) show a rough estimate of this error in the form of a dimensionless capillary number Ca, evaluated for a limited range of Laplace numbers La (using the macroscopic density (Eq. (19)) and viscosity (Eq. (20))):

$$Ca = \frac{\eta |\mathbf{u}|_{max}}{\sigma} \qquad (25)$$

$$La = \frac{\rho \sigma d}{\eta^2} \qquad (26)$$

Our simulations, which have been carried out over a wide range of Laplace numbers, show a similar error of $O(10^{-3})$ for the classic Eulerian treatment of the pressure jump. The improvement by means of the new method to account for the pressure jump reduces this error by two orders of magnitude , which agrees with the instantaneous error in the momentum (Fig. 8, right). Secondly, it was found that when using the traditional Eulerian treatment of the pressure jump, the error depends only on the Eulerian grid size and not on the number of markers. This is conclusive evidence that the main problem of the traditional FT implementation is in the treatment of the pressure jump and not the accuracy of the surface tension model, as was first pointed out by Scardovelli and Zaleski (1999). By using the new and more accurate treatment of the pressure jump at the interface FT can significantly outperform other models, which makes it possible to run calculations with very high surface tension forces on relatively coarse grids.

Next to a quantitative difference, there is also a qualitative difference in the spurious currents around the bubble, as illustrated in Fig. 9 (velocity vectors not on the same scale). It can be seen that the traditional implementation gives erratic velocity vectors at the interface, while the improved version has a clear circulation pattern inside the bubble. Both are, however, divergence free.

### 3.2. Standard advection test

The advection of the interface is studied using a standard advection test (following Rider and Kothe, 1998), which involves a bubble with radius $\frac{1}{4}$ at a dimensionless position $(\frac{1}{2}, \frac{1}{2}, \frac{3}{4})$ in a rotational velocity field given by

$$\mathbf{u}(x,y,z) = (0, -2\sin^2(\pi y)\sin(\pi z)\cos(\pi z), 2\sin^2(\pi z)\sin(\pi y)\cos(\pi y))$$
$$(27)$$

In this case a computational domain consisting of $30 \times 30 \times 30$ cells is used with 200 time steps of 0.01 s. The markers are between 0.2 and 0.4 times the size of the Eulerian grid size, and the bubble contains 10 Eulerian cells. Further physical properties are irrelevant because the flow field is given. Because the velocity field is divergence free, and the markers on the interface move with the interpolated fluid velocity, the bubble volume should always be conserved. Secondly, after reversing the velocity field

**Table 2**
Literature values for the maximum steady-state spurious currents around a perfect sphere.

| Source | $d/\Delta x$ | La | Ca |
|---|---|---|---|
| de Sousa et al. (2004) | 12.5, 25 | 250 | $O(10^{-3}), O(10^{-4})$ |
| Singh and Shyy (2007) | – | 250–12 000 | $O(10^{-4})$ |
| This work | $\geq 10$ | 1–10 000 | $< 2.2 \times 10^{-5}$ |
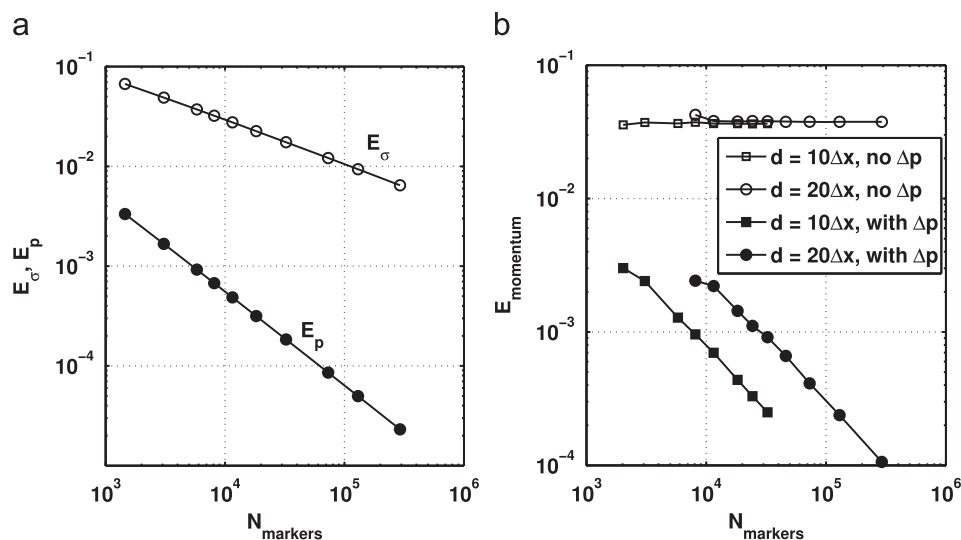


**Fig. 8.** (a) $L_2$–error norm for the surface tension force on a single marker and the interfacial pressure jump as a function of the number of markers $N_m$ and (b) dimensionless false momentum as a result of the mismatch between surface tension forces and interfacial pressure jump, as a function of the number of markers. For two different resolutions, we have given the results for simulations with and without pressure jump handling as described in Section 2.3.
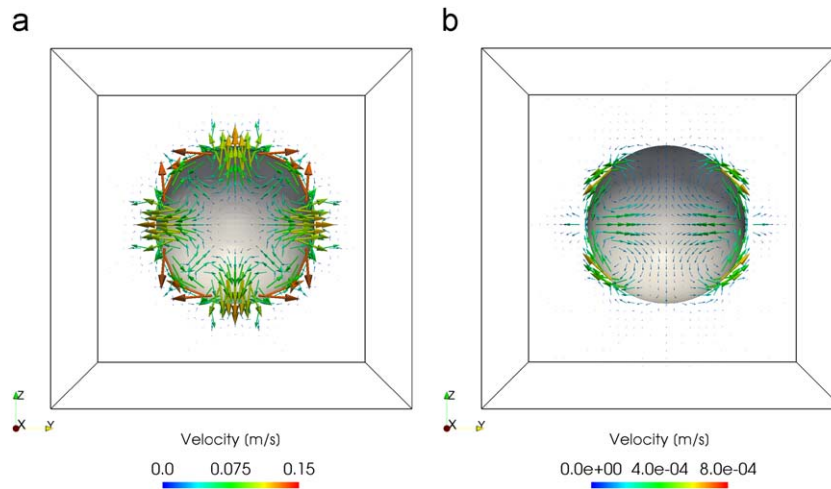
**Fig. 9.** Spurious vector field around the central slice of a spherical air bubble with $d = 1$ mm. It can be seen that the standard Eulerian pressure treatment (left) gives many erratic vectors at certain locations on the interface, while the new implementation to account for the pressure jump at the interface (right) yields a much smaller and symmetric circulation pattern. The size of the vectors of a and b differ by a factor 200 for visibility.

**Table 3**
Errors in the standard advection test for different advection schemes ($V$ = bubble volume; $\mathbf{x}$ = dimensionless bubble position).

| Numerical scheme | | | $t = 1$ s | $t = 2$ s | |
|---|---|---|---|---|---|
| Interpolation | Time stepping | Remeshing | $(V - V_0)/V_0$ | $(V - V_0)/V_0$ | $\mathbf{x} - \mathbf{x}_0$ |
| Linear | Euler | – | $-9.71 \times 10^{-3}$ | $-3.36 \times 10^{-2}$ | $6.93 \times 10^{-2}$ |
| Linear | Runge–Kutta | – | $-8.51 \times 10^{-4}$ | $1.48 \times 10^{-8}$ | $2.03 \times 10^{-9}$ |
| Spline | Euler | – | $-9.88 \times 10^{-3}$ | $-3.41 \times 10^{-2}$ | $6.99 \times 10^{-2}$ |
| Spline | Runge–Kutta | – | $-8.55 \times 10^{-4}$ | $1.44 \times 10^{-8}$ | $2.03 \times 10^{-9}$ |
| Linear | Euler | X | $-1.37 \times 10^{-2}$ | $-4.27 \times 10^{-2}$ | $6.92 \times 10^{-2}$ |
| Spline | Runge–Kutta | X | $-4.76 \times 10^{-3}$ | $8.92 \times 10^{-3}$ | $2.72 \times 10^{-4}$ |

halfway (after 1 s), the bubble should return exactly to its starting position. However, due to the finite accuracy of the numerical schemes used, there can be an error in the volume, final location and shape of the bubble. The errors in the location and volume of the bubble are analyzed quantitatively in Table 3.

We first consider the cases without remeshing. Considering the volume loss at $t = 2$ s, the Runge–Kutta time integration reduces all errors by a factor of one million, regardless of the method for the velocity interpolation used. A more interesting result is found half-way the advection test (at $t = 1$ s). A significantly larger volume loss is observed (despite the R–K timestepping procedure). Because the remeshing is not active, the Lagrangian control points are moved increasingly further away from each other, hereby creating volume defects. Because the bubble volume is analytically calculated from the triangular, flat markers between three Lagrangian control points, concave parts from the bubble gain volume, whereas convex parts of the interface lose volume. When the flow field has reversed, the points move towards each other again, hereby restoring the bubble volume to a large extend. This demonstrates the need for remeshing. A higher order velocity interpolation (third order spline) is still important in order to keep the bubble surface smooth (Fig. 2).

Remeshing procedures also introduce volume defects, which result from a similar mechanism as presented above. Therefore, with the addition of remeshing, the error in the bubble volume rises significantly, but it can be seen that the higher order advection still improves the volume conservation.

The shape of the bubbles together with the streamlines are shown in Fig. 10. It can be seen that for the standard Euler time

integration with linear interpolation, the bubble shape at the end of the test is moved away from its initial position, while for the higher order interpolation and time stepping the interface is found exactly on top of the initial bubble. All together, a higher order interpolation of the velocity (spline) and Runge–Kutta timestepping, combined with a remeshing function, produce very satisfying results.

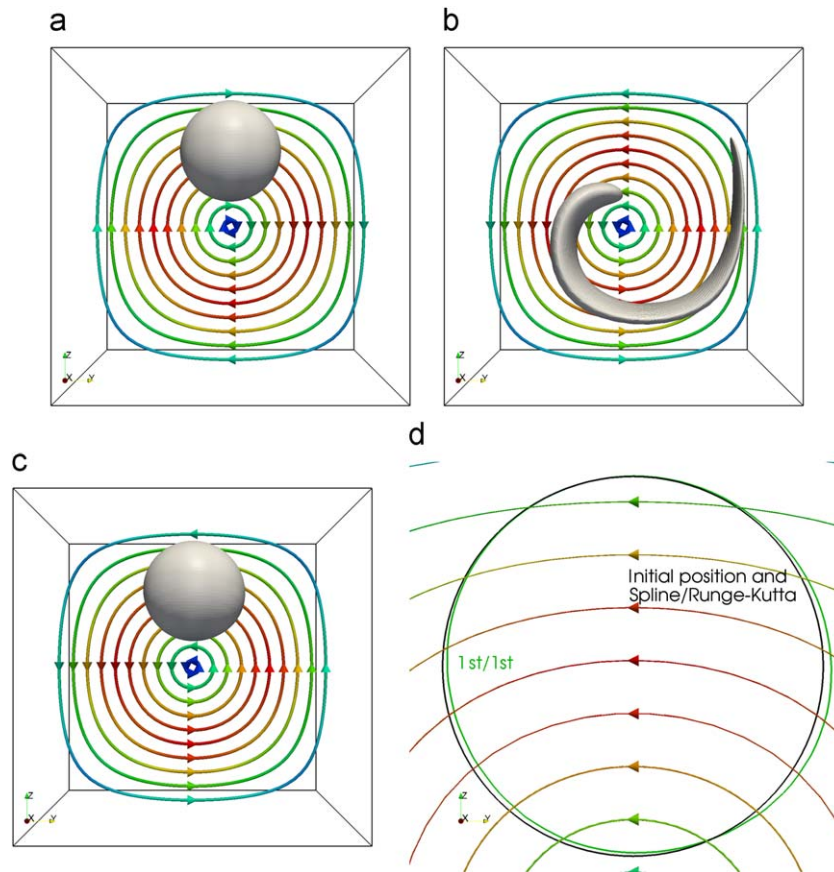### 3.3. Oscillating drop with viscous damping

In order to verify the correct interchange between the surface tension force and momentum, an initially slightly prolate droplet in a zero-gravity field is simulated. The droplet will oscillate as a result of the surface tension force. The droplet diameter can be calculated over time using Eq. (28) (Lamb, 1932). In this equation, $\omega$ stands for the analytical solution for the frequency of the lowest mode, calculated by Eq. (29). The viscous damping of the initial amplitude $a_0$ can be described by Eqs. (30) and (31).

$$d(t) = d_0 + a_0 \exp\left(-\frac{t}{\tau}\right)\cos(\omega t) \tag{28}$$

$$\omega^2 = \frac{24\sigma}{(3\rho_d + 2\rho_c)\left(\frac{d}{2}\right)^3} \tag{29}$$

$$a(t) = a_0 \exp\left(-\frac{t}{\tau}\right) \tag{30}$$

**Fig. 10.** The first three images show the evolution of the advection test. At $t = 0$ s, the bubble is subjected to a rotational flow and deformed. At $t = 1$ s, the bubble is deformed and the flow is reversed. At $t = 2$ s, the bubble should have returned to its initial position. The d shows a cut-plane of the bubble at $t = 2$ s. Using spline interpolation and Runge–Kutta time integration the bubble returns completely to its initial position (black line), while using first order interpolation and first order time integration, the bubble is slightly shifted (green line): (a) snapshot at $t = 0$ s, (b) $t = 1$ s, (c) $t = 2$ s and (d) difference between first order and higher order advection. (For interpretation of the references to the colour in this figure legend, the reader is referred to the web version of this article.)

**Table 4**
Physical and numerical settings for the oscillating drop case.

| Property (dimensionless) | Value |
|---|---|
| Domain size | $20 \times 20 \times 20$ |
| | $40 \times 40 \times 40$ |
| Grid size $\Delta x$ | 0.2 |
| | 0.1 |
| Time step $\Delta t$ | $5 \times 10^{-3}$ |
| Equivalent drop diameter $d_0$ | 2 |
| Initial amplitude $a_0$ | 0.05 |
| Dispersed phase density $\rho_d$ | 100 |
| Dispersed phase viscosity $\eta_d$ | 0.35 |
| Continuous phase density $\rho_c$ | 1 |
| Continuous phase viscosity $\eta_c$ | $1 \times 10^{-3}$ |
| Surface tension coefficient $\sigma$ | 10 |

$$\tau = \frac{\rho_d d}{10 \eta_d} \tag{31}$$

To be able to compare the model results with this analytical solution, a system is selected with a low viscosity and density for the continuous phase (Table 4), so that the effect of the surrounding fluid can be neglected. Two resolutions of the droplet have been investigated, see Table 4. It can be seen from Fig. 11 that there is a very good agreement between the numerical results and the analytical solution. The period of the oscillation is

perfectly reproduced with an error of 1.28% on average over the simulated time shown in the figure.

## 4. Conclusions

In this article, the improvements made to a 3D front tracking code have been described and their effects were benchmarked. First a new method to account for the pressure jump in front tracking models is described and it has been shown that this method reduces the spurious currents by two orders of magnitude and solves volume loss issues for small bubbles with high surface tension forces. Secondly, the interface advection has been improved (higher order velocity interpolation and time stepping), resulting in less volume conservation errors and a noticeably smoother interface. Finally, the time step constraint for viscous liquids was overcome by using a semi-implicit treatment of the stress tensor in the Navier–Stokes equations.

## Notation

| | |
|---|---|
| $a$ | amplitude, m |
| Ca | capillary number, dimensionless |
| $d$ | equivalent bubble diameter, m |
| $d_x, d_y, d_z$ | distribution functions in one direction, dimensionless |
| $D$ | volume weighing distribution kernel, dimensionless |
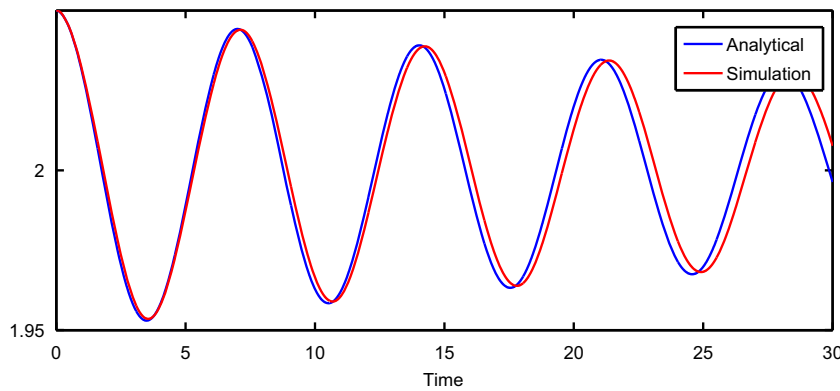
**Fig. 11.** Bubble diameter for an oscillating drop with viscous damping, simulated with $d = 20\Delta x = 2$. The error in the oscillation period was 1.28%, calculated from the local minima and maxima.

| $\mathbf{e}_z$ | unit vector in the $z$-direction, dimensionless |
|---|---|
| $E$ | error, dimensionless |
| $F$ | force, N |
| $F_p$ | phase fraction, dimensionless |
| $\mathbf{g}$ | gravitational acceleration (in $z$ direction), $\mathrm{m\,s^{-2}}$ |
| $\mathbf{G}_p$ | gradient of the phase fraction, dimensionless |
| $h$ | mesh spacing, m |
| $i, j, k$ | discrete Cartesian coordinates, m |
| La | Laplace number, dimensionless |
| $\mathbf{n}$ | unit normal vector, dimensionless |
| $N$ | number of cells, dimensionless |
| $N_m$ | number of markers, dimensionless |
| $N_{ph}$ | number of phases, dimensionless |
| $p$ | pressure, Pa |
| $\Delta p$ | pressure jump, Pa |
| Re | Reynolds number ($\mathrm{Re} = \rho_c |\mathbf{v} - \mathbf{u}| d \eta_c^{-1}$), dimensionless |
| $S$ | surface area, $\mathrm{m^2}$ |
| $t$ | time, s |
| $\mathbf{t}$ | tangent vector, m |
| $\Delta t$ | time step, s |
| $\mathbf{u}$ | continuous phase velocity, $\mathrm{m\,s^{-1}}$ |
| $\mathbf{v}$ | dispersed phase velocity, $\mathrm{m\,s^{-1}}$ |
| $V$ | volume, $\mathrm{m^3}$ |
| $x, y, z$ | Cartesian coordinates, m |
| $\mathbf{x}$ | position, m |

*Greek letters*

| $\delta p$ | pressure correction, Pa |
|---|---|
| $\eta$ | dynamic viscosity, Pa s |
| $\rho$ | density, $\mathrm{kg\,m^{-3}}$ |
| $\sigma$ | surface tension coefficient, $\mathrm{N\,m^{-1}}$ |
| $\tau$ | characteristic time, s |
| $\boldsymbol{\tau}$ | stress tensor, $\mathrm{N\,m^{-2}}$ |
| $\omega$ | oscillation period, s |

*Super/subscripts*

| $d$ | dispersed phase |
|---|---|
| $c$ | continuous phase |
| $h$ | horizontal direction |
| $m$ | marker |
| $max$ | maximum |
| $n$ | current time-level |
| $n^*, n^{**}$ | intermediate time-level |
| $n+1$ | new time-level |

| $p$ | phase or pressure |
|---|---|
| th | theoretical |
| $v, z$ | vertical direction |
| $x, y$ | horizontal direction |
| 0 | initial value |
| $\sigma$ | surface tension |

## Acknowledgements

## References

Brackbill, J.U., Kothe, D.B., Zemach, C., 1992. A continuum method for modeling surface tension. Journal of Computational Physics 100 (2), 335–354, doi:10.1016/0021-9991(92)90240-Y.

Centrella, J., Wilson, J.R., 1984. Planar numerical cosmology. II—the difference equations and numerical tests. Astrophysical Journal Supplement Series 54, 229–249.

Deen, N.G., van Sint Annaland, M., Kuipers, J.A.M., 2004. Multi-scale modeling of dispersed gas–liquid two-phase flow. Chemical Engineering Science 59 (8–9), 1853–1861, doi:10.1016/j.ces.2004.01.038.

Dijkhuizen, W., 2008. Derivation of closures for bubbly flows using direct numerical simulations, Ph.D. Thesis, University of Twente.

de Sousa, F.S., Mangiavacchi, N., Nonato, L.G., Castelo, A., Tom, M.F., Ferreira, V.G., Cuminato, J.A., McKee, S., 2004. A front-tracking/front-capturing method for the simulation of 3D multi-fluid flows with free surfaces. Journal of Computational Physics 198, 469.

Francois, M.M., Cummins, S.J., Dendy, E.D., Kothe, D.B., Sicilian, J.M., Williams, M.W., 2006. A balanced-force algorithm for continuous and sharp interfacial surface tension models within a volume tracking framework. Journal of Computational Physics 213 (1), 141–173, doi:10.1016/j.jcp.2005.08.004.

Lamb, H., 1932. Hydrodynamics, sixth ed. Cambridge University Press, London.

Peskin, C.S., 1977. Numerical analysis of blood flow in the heart. Journal of Computational Physics 25 (3), 220–252, doi:10.1016/0021-9991(77)90100-0.

Popinet, S., Zaleski, S., 1999. A front-tracking algorithm for the accurate representation of surface tension. International Journal for Numerical Methods in Fluids 30, 775.

Press, W.H., Vetterling, W.T., 1992. Numerical Recipies in C. Cambridge University Press, Cambridge.

Prosperetti, A., 2002. Navier–Stokes numerical algorithms for free-surface flow computations: an overview. Drop-surface interaction 237.

Renardy, Y., Renardy, M., 2002. PROST: a parabolic reconstruction of surface tension for the volume-of-fluid method. Journal of Computational Physics 183 (2), 400–421, doi:10.1006/jcph.2002.7190.

Rider, W.J., Kothe, D.B., 1998. Reconstructing volume tracking, Journal of Computational Physics 141, 112. doi:10.1006/jcph.1998.5906.

Scardovelli, R., Zaleski, S., 1999. Direct numerical simulation of free-surface and interfacial flow. Annual Review of Fluid Mechanics 31, 567.

Shin, S., Juric, D., 2002. Modeling three-dimensional multiphase flow using a level contour reconstruction method for front tracking without connectivity. Journal of Computational Physics 180, 427.

Singh, R., Shyy, W., 2007. Three-dimensional adaptive Cartesian grid method with conservative, interface restructuring and reconstruction. Journal of Computational Physics 224, 150–167.

Tryggvason, G., Bunner, B., Esmaeeli, A., Juric, D., Al-Rawahi, N., Tauber, W., Han, J., Nas, S., Jan, Y.J., 2001. A front-tracking method for the computations of multiphase flows. Journal of Computational Physics 169, 708.

Uhlmann, M., 2005. An immersed boundary method with direct forcing for the simulation of particulate flows. Journal of Computational Physics 209, 448–476.

Unverdi, S.O., Tryggvason, G., 1992. A front tracking method for viscous, incompressible, multi-fluid flows. Journal of Computational Physics 100, 25.

van Sint Annaland, M., Dijkhuizen, W., Deen, N.G., Kuipers, J.A.M., 2006. Numerical simulation of gas bubbles behaviour using a 3D front tracking method. A.I.Ch.E. Journal 52, 99.

Zaleski, S., 2005. Interface Tracking VOF, in: Von Karman Institute for Fluid Mechanics, Belgium.